Christian FRIEDRICH[1,2*]
Steffen IHLENFELDT[1,2]

SPATIAL COMPLIANCE MEASUREMENT OF A CLAMPING TABLE WITH INTEGRATED FORCE SENSORS

Force sensor integration into machine components is a promising approach to measure spatial process forces, especially, when regarding hexapod structures and kinematics. Rigid still-standing hexapod frameworks, such as clamping tables, are particular suitable for this approach, as no dynamic influences need to be taken into account within the measurement model and they allow a measurement in 6 degrees of freedom. On the other hand, the stiffness of rigid frameworks is reduced by force sensor integration significantly. In addition, many approaches apply joints or flexure hinges to reduced lateral forces and improve the measuring quality, which reduce the stiffness even more. In this contribution, the compliance of a clamping table with integrated force sensors and flexure hinges is determined by experimental measurements using a multiline laser interferometer, by analytic calculation, and by finite element simulation. In conclusion, the amount of stiffness reduction by force sensors and flexure hinges is quantified and different methods for compliance determination are compared.

1. INTRODUCTION AND APPROACH

Today, many manufacturing applications require in-process measurement of forces and moments, such as process diagnosis and monitoring, quality assurance, or adaptive process control. With the extended movability of modern machine tools, such as five-axis kinematics or hexapods, the measurement of *spatial* forces and moments in up to 6 degrees of freedom (DoF) is requested in particular. Hereby, force sensor integration into hexapod structures and kinematics is particularly suitable for the reasons of 6 DoF- and nearly frictionless measurement as well as lightweight design. Because no dynamic influences need to be taken into account, rigid unmoved bar frameworks, e.g. clamping tables, are advantageous with regard to low modelling effort to obtain the measurement model and, therefore, the preferred solution in the state of the art, Fig. 1.

First contributions that use Stewart or hexapod structures as force sensors were presented in the 80s and 90s [1–6]. In the following years, the topic has been studied further

_____

[1] Institute of Mechatronic Engineering, Chair of Machine Tools Development and Adaptive Controls, TU Dresden, Germany
[2] Fraunhofer Institute for Machine Tools and Forming Technology, Dresden, Germany
[*] E-mail: Christian.Friedrich@iwu.fraunhofer.de

[7–9], including first finite element simulations [10, 11] and first evaluations on flexure hinges [12, 13]. The most promising actual works show application-oriented results, such as a multicomponent calibration system [14, 15], a sensor for heavy duty applications [16–19], an endoscope with integrated force measurement for minimal invasive surgery [20, 21], or a measuring system for industrial applications [22]. Further, the approach has been evolved to moving hexapod structures and hexapod kinematics [23–27].

Fig. 1. Hexapod-based clamping table with integrated force sensors and flexure hinges (left); Details on mechanical design with sensors and flexure hinges (right, top), with sensors only (right, mid), and without sensors (right, bottom)

Nevertheless, two main aspects are not discussed in the state of the art: Firstly, the stiffness loss due to the force sensor integration, when compared to rigid frameworks and, secondly, a comparison of methods for simple compliance evaluation in design stage. As the used force sensors are based on strain gauges, they can be regarded as springs, which may reduce the stiffness of rigid frameworks significantly. In addition, many approaches use joints or flexure hinges to reduced lateral forces, which cannot be measured by the force sensors, to improve the measuring quality [12, 15]. In the consequence, the stiffness of the frame is reduced even more, which contradicts the general demands of high accuracy and stiffness in machine tool industry. For the force sensor integration into a hexapod machine tool, the resulting loss of stiffness is very limited (5–10%), as the sensor stiffness is much higher than the stiffness of other components, such as the drive train [26].

However, the effective amount of stiffness reduction due to force sensor integration in rigid bar frameworks and the influence of the flexure hinges are open research questions. The new contribution of this paper is the compliance evaluation of a hexapod-based clamping table in three configurations that include force sensors and flexure hinges by different methods. At first, the three used methods for compliance evaluation are introduced (Section 2) and, next, the resulting compliances as well as the methods are assessed (Section 3).

2. METHODS

To evaluate the compliance of the rigid hexapod-based clamping table, three methods are evaluated and compared: first, the experimental evaluation by load application and displacement measurement (Section 2.1), second, the analytic calculation by serial and parallel connection of the component compliances (Section 2.2), and, third, the computational calculation by finite elements (FE) simulation (Section 2.3).

The clamping table consists of six identical legs with individual lengths that allow for an individual configuration of its pose (position and orientation) with respect to the application, Fig. 1. The steel bars are made of hydraulic pipes with an inner diameter of 30 mm and an outer diameter of 38 mm in which M20 thread rods are screwed-in. At the top as well as at the bottom, ball heads for clamping are screw-in or welded-on, respectively. Multiple configurations of the table with (wS) and without (oS) force sensors as well as with (wH) and without (oH) flexure hinges are modelled and built. Figure 2. summarises the evaluated variants in CAD and FEM drawings. Because all connections are clamped or welded, the initial framework without sensors and flexure hinges (oSoH) will be regarded as rigid and the evaluations are made with respect to this initial state. Force sensor are integrated by the use of M12 external threads and adequate adapter pieces. Flexure hinges are realised by reducing the rod diameter from 22 mm to 6 mm, Fig. 2 right.
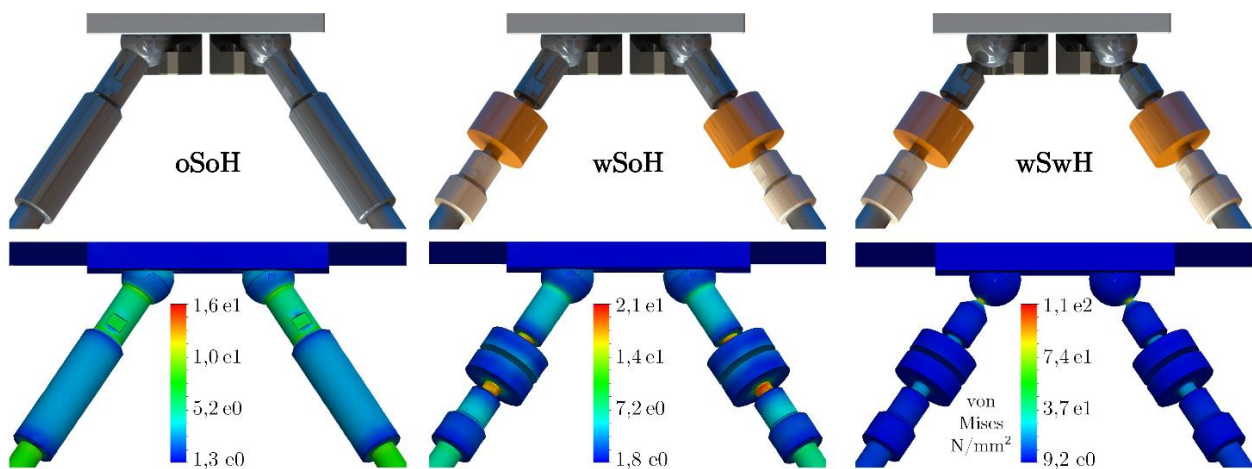

Fig. 2. Details of Axis 5 and 6 of the clamping table in CAD (top) and FE model (bottom) in the variants: without force sensors without flexure hinges (oSoH), with force sensors without flexure hinges (wSoH) and with forces sensors with flexure hinges (wSwH)

2.1. EXPERIMENTAL EVALUATION

At first for experimental compliance evaluation, forces are applied to the clamping table by a hexapod machine tool, Fig. 3 left, and the resulting displacements are measured with the help of the absolute laser interferometer Etalon Multiline, Fig. 3 right. The setup for the displacement measurement including lasers and reflectors is presented in Fig. 4.
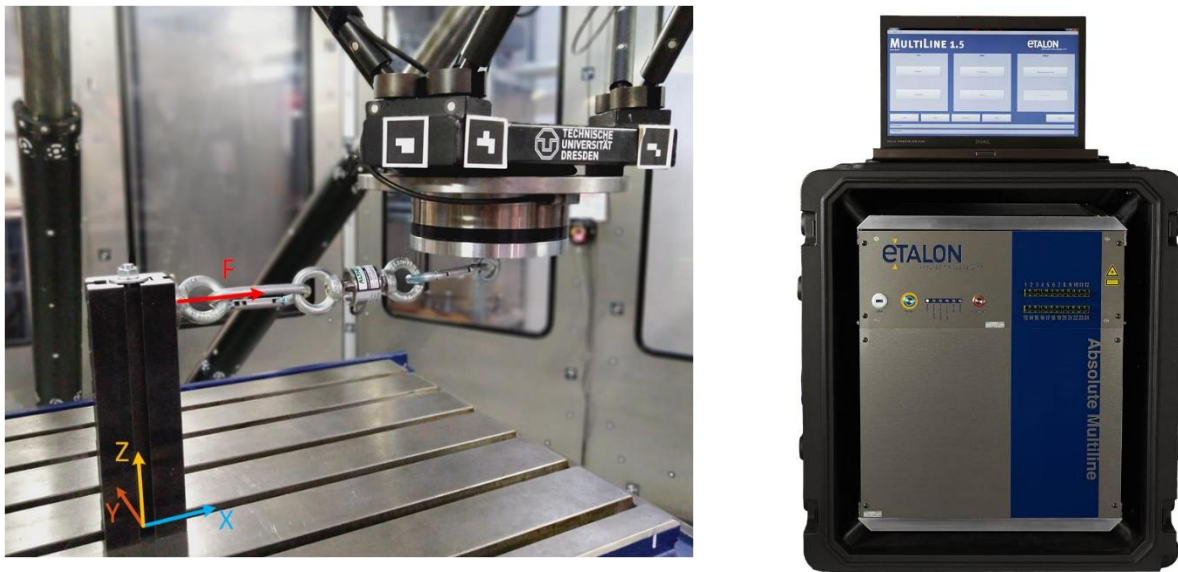
Fig. 3. Force application to the clamping table with the help of a hexapod machine tool (left) and displacement measurement with the Etalon Multiline absolute laser interferometer (right) [28]
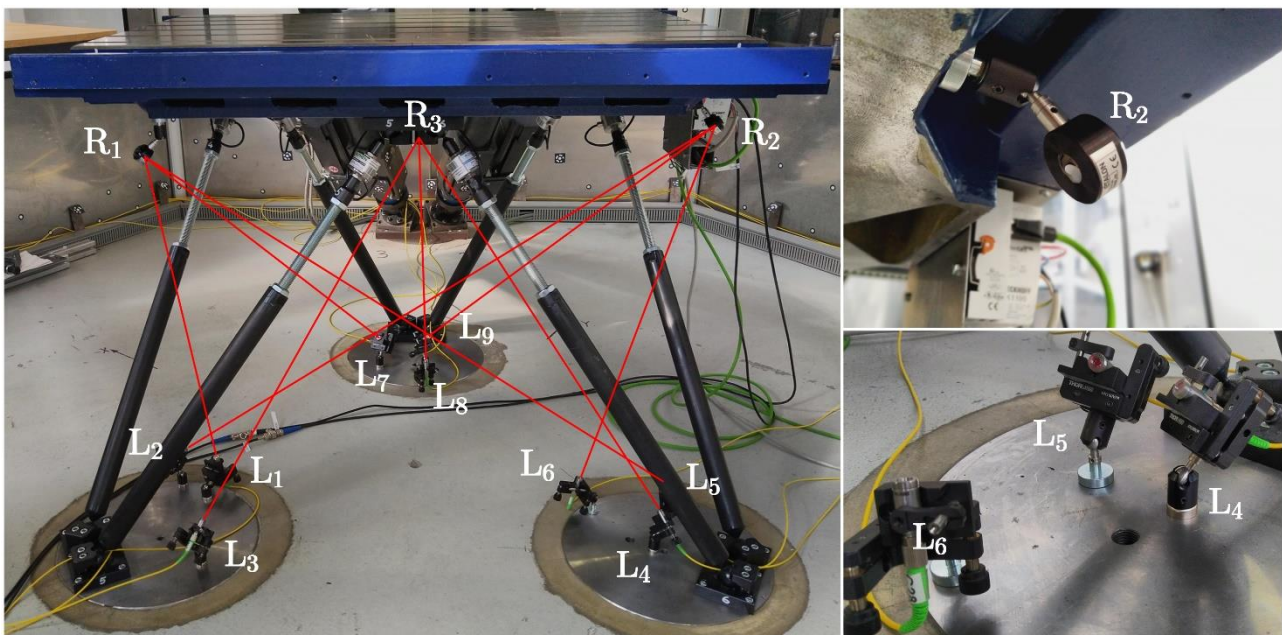

Fig. 4. Laser and reflector configuration for spatial displacement measurement of the clamping table (wSwH), 9 laser collimators (L) and 3 reflectors (R)

As shown by Eq. (1), a position change of the hexapod machine tool $\Delta \boldsymbol{p}_{\text{Hex}}$ results in a spatial force applied to the clamping table $\Delta \underline{\boldsymbol{f}}_T$, which reacts according to its compliance $\boldsymbol{N}_T$ with a displacement $\Delta \underline{\boldsymbol{x}}_T$ that finally can be detected by changing laser lengths $\Delta \boldsymbol{l}$.

$$\Delta \boldsymbol{p}_{\text{Hex}} \xrightarrow{\boldsymbol{K}_{\text{Hex}}} \Delta \underline{\boldsymbol{f}}_T \xrightarrow{\boldsymbol{N}_T} \Delta \underline{\boldsymbol{x}}_T \xrightarrow{RT_{\text{Laser}}} \Delta \boldsymbol{l}. \tag{1}$$

The requested compliance of the framework N_T can be obtained in two steps. First, the pose change of the table $\Delta \underline{x}_T$ is calculated from the change of the laser lengths Δl for every load situation. To do so, a Jacobian matrix is requested that fulfils $\Delta l = J_L^{-1} \Delta \underline{x}_T$, which can be found by geometric analysis of the setup, Fig. 5.
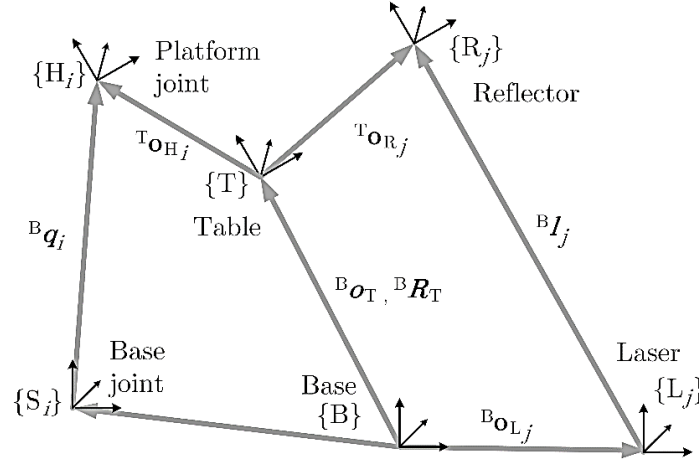

Fig. 5. Modelling of table and laser kinematics

The inverse problem RT_{Laser} that describes the vector of the laser beam j on the base of the position ($^B o_T$) and orientation ($^B R_T$) of the table platform calculates for all $j = 1 ... 9$ lasers to

$$^B l_j = {}^B o_T + {}^B R_T\, {}^T o_{Rj} - {}^B o_{Lj}. \tag{2}$$

The derivation of Eq. () with respect to time leads to the geometric Jacobian $J_L^{-T\ (6\times 9)}$ of the setup

$$J_L^{-T} = \begin{pmatrix} n_1 & ... & n_9 \\ h_1 \times n_1 & ... & h_9 \times n_9 \end{pmatrix} \tag{3}$$

based on the vectors $^B n_j$ und $^B h_j$ that are defined by the placement of the collimators and reflectors in non-deformed state ($\{B\} \triangleq \{T\}$) as following:

$$\begin{aligned} ^B n_j &= ({}^{B=T} o_{Rj} - {}^B o_{Lj})/|\,^B l_j| \\ ^B h_j &= {}^{B=T} o_{Rj}. \end{aligned} \tag{4}$$

Due to the relative measurement of the deformed state related to the original state, these coordinates do not need to be precise. On the contrary, a rough estimate with an accuracy of approx. 5 mm is sufficient, see Table 1 right. Also, the change of the Jacobian due to the deformation can be neglected.

Finally, the best estimate of the pose change $\Delta \widehat{\underline{x}}_T$ is obtained by least squares, after including the measurements $\Delta \check{l}$ with

$$\Delta \widehat{\underline{x}}_T = (J_L^{-1} J_L^{-T})^{-1} J_L^{-1} \Delta \check{l}. \tag{5}$$

The result contains position and orientation in the form $\Delta\widehat{\underline{x}}_\text{T} = \left(^\text{B}\boldsymbol{o}_\text{T}^{\ T}\ ^\text{B}\boldsymbol{\phi}_\text{T}^{\ T} \right)^T$, where the rotation matrix of the orientation can be approximated using $^\text{B}\boldsymbol{R}_\text{T} \approx \mathbf{1} + \boldsymbol{S}\left(^\text{B}\boldsymbol{\phi}_\text{T} \right)$ because of small angles. When using the pose definition $\left\{ ^\text{B}\boldsymbol{o}_\text{T}, \ ^\text{B}\boldsymbol{R}_\text{T} \right\}$ and the inverse transformation Eq. (2) the theoretical laser lengths can be calculated, which is used for validation.

Table 1. Coordinates of Base (S) and Platform points (H) of the clamping table as well as of the lasers (L) and reflectors (R) in mm, compare to Fig. 4

	Table Joint Positions				Laser/Reflector Positions		
	X	Y	Z		X	Y	Z
$^\text{B}\boldsymbol{o}_\text{S1}$	540.2	-281.2	-844.7	$^\text{B}\boldsymbol{o}_\text{L1}$	-370	-140	-763
$^\text{B}\boldsymbol{o}_\text{S2}$	43.9	591.1	-843.0	$^\text{B}\boldsymbol{o}_\text{L2}$	-435	-75	-758
$^\text{B}\boldsymbol{o}_\text{S3}$	-36.1	591.6	-842,7	$^\text{B}\boldsymbol{o}_\text{L3}$	-355	-300	-758
$^\text{B}\boldsymbol{o}_\text{S4}$	-543.4	-2743	-841.0	$^\text{B}\boldsymbol{o}_\text{L4}$	385	-245	-758
$^\text{B}\boldsymbol{o}_\text{S5}$	-503.8	-3438	-841,1	$^\text{B}\boldsymbol{o}_\text{L5}$	415	-205	-758
$^\text{B}\boldsymbol{o}_\text{S6}$	499.7	-350.2	-844.6	$^\text{B}\boldsymbol{o}_\text{L6}$	285	-155	-763
$^\text{T}\boldsymbol{o}_\text{H1}$	383.5	284.7	-153.7	$^\text{B}\boldsymbol{o}_\text{L7}$	35	425	-758
$^\text{T}\boldsymbol{o}_\text{H2}$	303.5	284.7	-153.7	$^\text{B}\boldsymbol{o}_\text{L8}$	40	310	-763
$^\text{T}\boldsymbol{o}_\text{H3}$	-296.5	284.7	-153.7	$^\text{B}\boldsymbol{o}_\text{L9}$	-95	435	-758
$^\text{T}\boldsymbol{o}_\text{H4}$	-376.5	284,7	-153.7	$^\text{T}\boldsymbol{o}_\text{H1}$	-440	-145	-183
$^\text{T}\boldsymbol{o}_\text{H5}$	-36.5	-105.3	-148.7	$^\text{T}\boldsymbol{o}_\text{H1}$	475	-110	-133
$^\text{T}\boldsymbol{o}_\text{H6}$	435	-1053	-148.7	$^\text{T}\boldsymbol{o}_\text{H1}$	15	430	-133

In the second step, the compliance matrix $\boldsymbol{N}_\text{T}$ is calculated using all load situations $\Delta\breve{\underline{\boldsymbol{f}}}_{\text{T},l}$ and their corresponding identified displacements $\Delta\widehat{\underline{\boldsymbol{x}}}_{\text{T},l}$ in a way that fulfils for every load situation $l = 1 \dots \text{m}$ the compliance model

$$\Delta\widehat{\underline{\boldsymbol{x}}}_{\text{T},l} = \boldsymbol{N}_\text{T}\Delta\breve{\underline{\boldsymbol{f}}}_{\text{T},l}. \tag{6}$$

To identify the unknown elements $n_{\text{T},ij}$ of $\boldsymbol{N}_\text{T}$, Eq. (6) is converted to the following form, where the unknowns appear as vector $\boldsymbol{n}_\text{T}$.

$$\Delta\widehat{\underline{\boldsymbol{x}}}_{\text{T},l} = \breve{\boldsymbol{F}}_{\text{T},l}\boldsymbol{n}_\text{T} = \begin{pmatrix} \Delta\breve{\underline{\boldsymbol{f}}}_{\text{T},l}^T & \mathbf{0} & \mathbf{0} & \mathbf{0} & \mathbf{0} & \mathbf{0} \\ \mathbf{0} & \Delta\breve{\underline{\boldsymbol{f}}}_{\text{T},l}^T & \mathbf{0} & \mathbf{0} & \mathbf{0} & \mathbf{0} \\ \mathbf{0} & \mathbf{0} & \Delta\breve{\underline{\boldsymbol{f}}}_{\text{T},l}^T & \mathbf{0} & \mathbf{0} & \mathbf{0} \\ \mathbf{0} & \mathbf{0} & \mathbf{0} & \Delta\breve{\underline{\boldsymbol{f}}}_{\text{T},l}^T & \mathbf{0} & \mathbf{0} \\ \mathbf{0} & \mathbf{0} & \mathbf{0} & \mathbf{0} & \Delta\breve{\underline{\boldsymbol{f}}}_{\text{T},l}^T & \mathbf{0} \\ \mathbf{0} & \mathbf{0} & \mathbf{0} & \mathbf{0} & \mathbf{0} & \Delta\breve{\underline{\boldsymbol{f}}}_{\text{T},l}^T \end{pmatrix} \begin{pmatrix} n_{\text{T},11} \\ \vdots \\ n_{\text{T},16} \\ n_{\text{T},21} \\ \vdots \\ n_{\text{T},26} \\ \vdots \end{pmatrix}. \tag{7}$$

Again, least squares lead to the best estimate of the unknowns after stacking models and measurements, with

$$\widehat{\boldsymbol{n}}_\text{T} = \left(\breve{\boldsymbol{F}}_\text{T}^T\breve{\boldsymbol{F}}_\text{T} \right)^{-1}\breve{\boldsymbol{F}}_\text{T}^T\Delta\widehat{\underline{\boldsymbol{x}}}_\text{T}. \tag{8}$$

The compliance matrix $\widehat{\boldsymbol{N}}_T$ is obtained by resorting $\widehat{\boldsymbol{n}}_T$, and the stiffness matrix $\widehat{\boldsymbol{K}}_T$ by inversion of $\widehat{\boldsymbol{N}}_T$.

Analogue to similar identification problems, observability indices and optimisation criteria can be used to plan and evaluate meaningful load situations, which maximise sensitivity and linear independency of the parameters with regard to the measurements [24]. In the presented application, the experiments are designed in a way that excites all components of the compliance matrix equally by symmetric distributed load situations, Table 2.

Table 2. Experimental plan and variation of the load situations

No.	Position in mm			Load Direction					
	X	Y	Z	X	Y	Z	A	B	C
1	40	0	0	+					
2	-40	0	0	−					
3	0	35	0		+				
4	0	-35	0		−				
5	0	0	0			+			
6	0	0	0			−			
7	40	0	230	+				+	
8	-40	0	230	−				−	
9	0	35	230		+		−		
10	0	-35	230		−		+		
11	300	0	0	−					−
12	300	0	0	+					+
13	300	0	0			+	+		
14	300	0	0			−	−		
15	300	0	230		−		+		−
16	300	0	230		+		−		+
17	0	300	0	+					−
18	0	300	0	−					+
19	0	300	0			+		−	
20	0	300	0			−		+	
21	0	300	230	+				+	−
22	0	300	230	−				−	+

The 22 experiments are performed for the presented variants of the clamping table (oSoH: without sensors and without flexure hinges, wSoH: with sensors and without flexure hinges, wSwH: with sensors and with flexure hinges) with one repetition. In doing so, the force is increased in 26 (wSwH) and 14 (wSoH, oSoH) steps, respectively, up to 2 kN and reduced in a similar manner. By the integrated force sensors (if present) and an additional force sensor, the applied forces are determined, where the applied moment results from the position of the force application due to the present lever, Table 2. The force measurement by the integrated force sensors in the clamping table allows for the determination of the lever by the twist and, therefore, a validation of the measuring setup.

Based on the control integration of the force and laser measurement, the experiments are fully automated: by the use of G-Code, the hexapod moves, which applies the force, and, after a short wait time, the force and laser measurements are triggered via M-commands.

2.2. ANALYTIC CALCULATION

Next, the table compliances shall be calculated analytically by serial and parallel connection of the component stiffnesses. As the longitudinal forces constitute the main influence in bar frameworks, the stiffness of one leg $k_{q,i}$ calculates from serial connection of the parts of the steel bar $k_{Steelbar}^{-1}$, the force sensor k_{Sensor}^{-1}, and two flexure hinges $k_{FlexHin}^{-1}$, if present

$$k_{q,i} = (k_{Steelbar\_bottom,i}^{-1} + k_{Steelbar\_top,i}^{-1} + k_{Sensor}^{-1} + 2\,k_{FlexHin}^{-1})^{-1}. \tag{9}$$

The used force sensors ALTHEN F256 5 kN have a longitudinal stiffness of $k_{Sensor} = 78$ N/µm, and the stiffness of the steel bars and flexure hinges can be taken from $k_i = EA_i/l_i$. Hereby, the diameters are $D = 18.38$ mm (M20 pitch diameter) and $D = 6$ mm (flexure hinges), respectively. l_i is either the length of bar $i = 1 \ldots 6$ or set to 2 mm for the flexure hinges, respectively.

To calculate the Cartesian stiffness $\boldsymbol{K}_x$ of the parallel-connected bars, the sensor directions need to be taken into account. This is performed by the use of the geometric Jacobian $\boldsymbol{J}_T$ of the table framework

$$\mathbf{J}_T^{-T} = \begin{pmatrix} \mathbf{n}_1 & \ldots & \mathbf{n}_6 \\ \mathbf{h}_1 \times \mathbf{n}_1 & \ldots & \mathbf{h}_6 \times \mathbf{n}_6 \end{pmatrix}, \tag{10}$$

Where, now, $\mathbf{n}_i$ is the unit vector that express the direction of force sensor i

$$^{B}\boldsymbol{q}_i = {}^{B}\boldsymbol{o}_T + {}^{B}\boldsymbol{R}_T\,{}^{T}\boldsymbol{o}_{Hi} - {}^{B}\boldsymbol{o}_{Si}.$$
$$\mathbf{n}_i = \boldsymbol{q}_i/|\boldsymbol{q}_i|, \tag{11}$$

and $\mathbf{h}_i$ is the corresponding lever with respect to the base frame $\{B\}$ [24]

$$\mathbf{h}_i = {}^{B}\boldsymbol{R}_T\,{}^{T}\boldsymbol{o}_{Hi}. \tag{12}$$

The positions of the joints ${}^{B}\boldsymbol{o}_{Si}$ and ${}^{T}\boldsymbol{o}_{Hi}$ are constant and can be easily obtained from mechanical design, compare Fig and Table left.

$$\boldsymbol{f}_x = \boldsymbol{J}_T^{-T}\boldsymbol{f}_q \tag{13}$$

Based on the static force transformation between sensor coordinates $\boldsymbol{f}_q$ and Cartesian coordinates $\boldsymbol{f}_x$, the derivation of Eq. (13) and insertion of Hooke's law with $\delta\boldsymbol{f}_q = \boldsymbol{K}_q\delta\boldsymbol{q}$ and $\delta\boldsymbol{f}_x = \boldsymbol{K}_x\delta\boldsymbol{x}$ leads, with $\delta\boldsymbol{q} = \boldsymbol{J}_T^{-1}\delta\boldsymbol{x}$, to the stiffness transformation

$$\boldsymbol{K}_x = \boldsymbol{J}_T^{-T}\boldsymbol{K}_q\,\boldsymbol{J}_T^{-1} + \boldsymbol{K}_{CCT}. \tag{14}$$

K_{CCT} is named Conservative Congruence Transformation [29] and can be neglected for stiff frameworks, as it describes the change of the Jacobian due to the deformation of the framework under load.

A representation of the distribution of measuring sensitivity and stiffness of the framework within the Cartesian space can be obtained by the sensitivity and stiffness hyper-ellipsoids: Inserting the force transformation $f_q = J_T^T f_x$ into a force unit sphere in sensor coordinates $f_q^T f_q = 1$ gives the Cartesian forces based on the sensor directions

$$f_x^T (J_T J_T^T) f_x = 1. \tag{15}$$

Hereby, the six-dimensional hyper-ellipsoid $J_T J_T^T$ represents the Cartesian sensitivity of the force measuring system. The stiffness hyper-ellipsoid can be produced in a similar manner: By inserting $\delta f_q = K_q \delta q$ into the static force transformation, the stiffness sphere $\delta q K_q^T K_q \delta q = 1$ results, and, finally, the stiffness hyper-ellipsoid [25]

$$\delta x^T J_T^{-T} K_q^T K_q J_T^{-1} \delta x = \delta x^T k_q^2 (J_T^{-T} J_T^{-1}) \delta x = 1. \tag{16}$$

For equal sensors and dominating longitudinal direction of action, the diagonal matrix K_q can be reduced to a scalar, and the stiffness hyper-ellipsoid is $k_q^2 (J_T J_T^T)^{-1}$, which is the inverse of the sensitivity hyper-ellipsoid. Finally for independent forces and moments, J_T can be split into two displayable three-dimensional ellipsoids for forces and moments [30]

$$f_q = J_{T,F}^T f_x + J_{T,M}^T m_x. \tag{17}$$

Figure 6 shows the resulting ellipsoids for the clamping table. The force ellipsoids $J_{T,F} J_{T,F}^T$ show a higher stiffness (lower sensitivity) in Z-direction, whereas the moment ellipsoids $J_{T,M} J_{T,M}^T$ indicate nearly homogeneous (sphere-like) behaviour in the rotational directions.
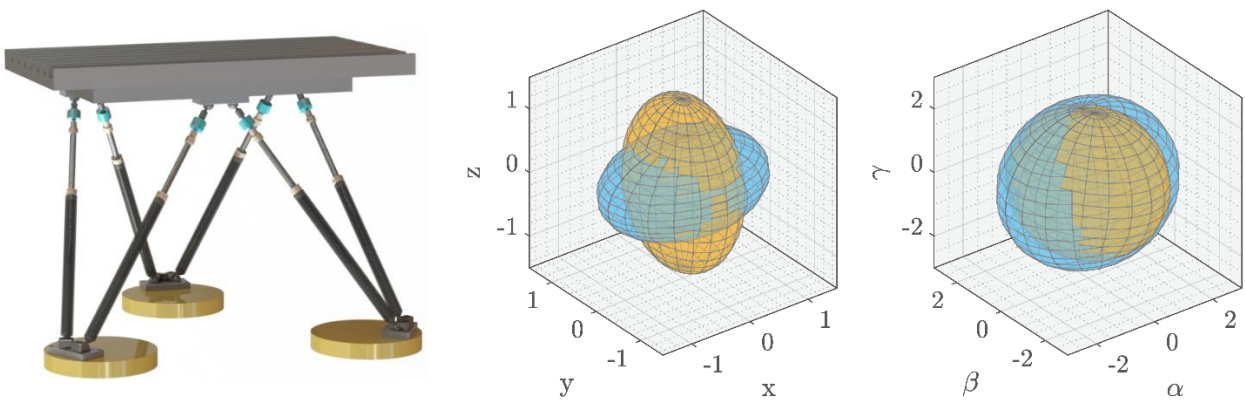

Fig. 6. Sensitivity (blue) and stiffness (yellow) ellipsoids for force (left) and moment (right) of the clamping table

The calculation of further technical values, such as range, resolution, or overload, as well as methods for the algorithmically optimisation of hexapod structures with integrated force sensors are presented in [25].

<center>2.3. FE-SIMULATION</center>

Finally, the table compliance shall be evaluated by finite elements simulation. The FE model bases on the CAD model of the table. In the first step, the design is simplified by eliminating irrelevant details, such as drill holes, to improve meshing quality and computation time. Next, boundary conditions with respect to the mounting of the components, e.g. the ball heads, are implemented, and multiple components are merged to obtain fewer parts. After introducing support conditions relative to the ground and parametrizing stiffnesses, e.g. for the force sensors, meshing and load application can be done.

Now, different load situations and the corresponding displacement measurements are implemented by the use of the FE-system Solidworks Simulation. The table compliance is evaluated in the same way as described for the experimental evaluation in Section 2.1 by simulating specific load situations according to the experimental plan in Table 2 and acquiring the resulting table displacement. Figure 7. shows exemplary results for the experiments 5 ($-Z$-load) and 20 ($-Z + B$-load), respectively, as wells as for the table configurations oSoH, wSoH, and wSwH. Finally, the spatial compliance matrix of the table is calculated from loads and displacements as described in Section 2.1.
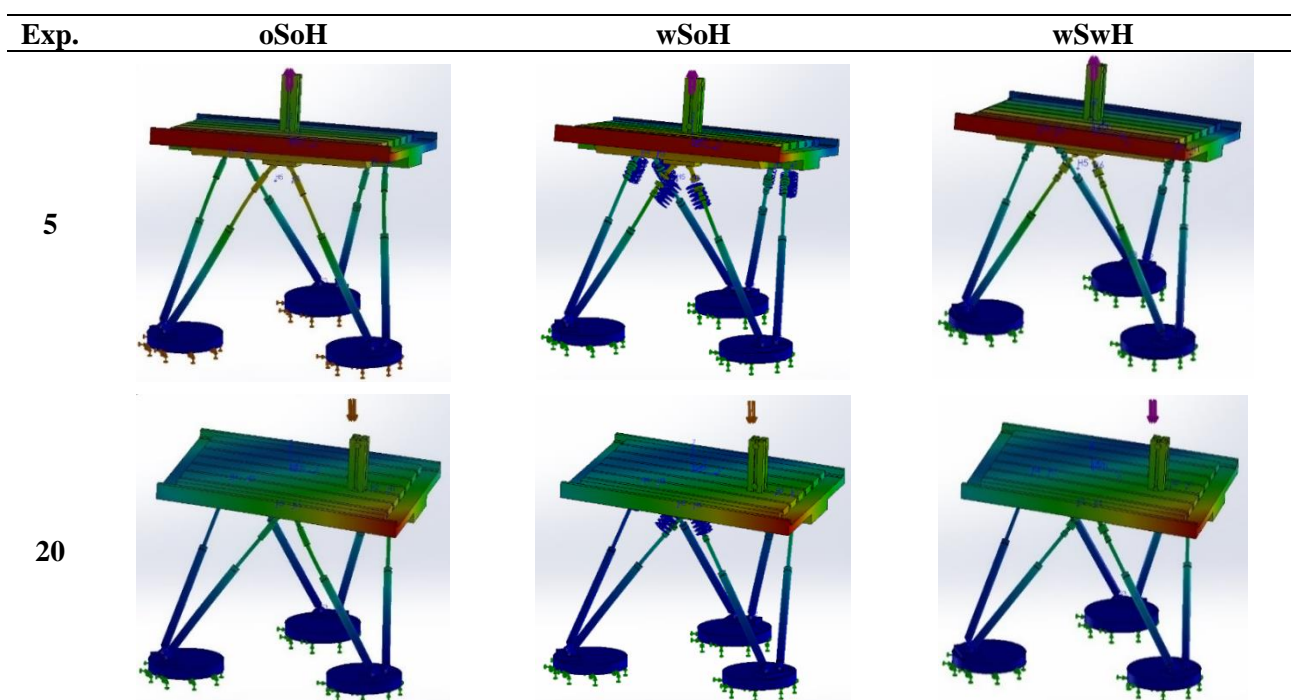

Fig. 7. Exemplary simulations with the FE-Model for different table setups and load situations (Exp: experiment, compare experimental plan in Table 2)

3. RESULTS

Figure 8 presents measuring results for forces and moments as wells as displacements on the example of the clamping table with force sensors and with flexure hinges (wSwH) in +X/+B direction (experiment 7). While the measured forces and moments match the direction

of their application, the direction of the displacement can be different due to non-diagonal components of the compliance matrix.

Further, the plot shows that in the practical setup non-linearity and hysteresis are very small and can be neglected, which is important to allow the extraction of meaningful compliances from the curves. Against this backdrop, and including force and displacement measurement in 6 DoF, small deviations in the experimental setup and force application are acceptable, and the compliance measurement is very robust.
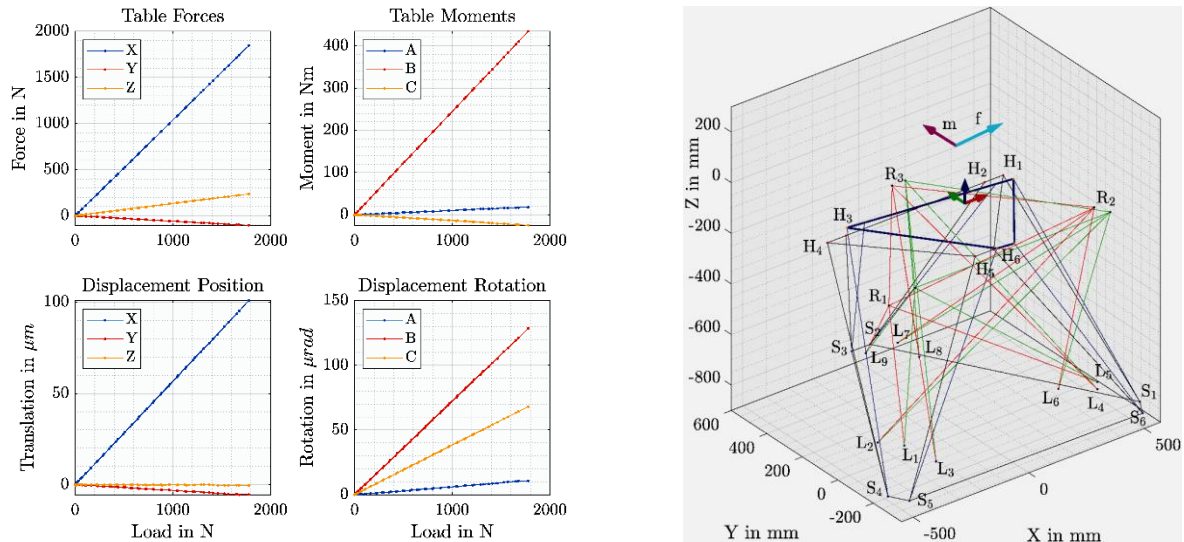

Fig. 8. Measuring results on the example of the clampling table with force sensors and with flexure hinges (wSwH) in +X/+B direction (experiment 7): left: measured forces and moments as well as identified displacements in position and orientation; right: spatial displacement at maximal force (black and red: table and lasers in start position, blue and green: table and lasers in deformed position)

With the use of the demonstrator hexapod machine tool Felix I, also other integrated force sensors in the end-effector platform (1b) and in the struts (2b) are available for comparison as well as the commercial force/torque sensor at the end-effector (R), see [25, 27]. As one additional result of the experimental studies, the various integrated force measuring systems do not lead to significant differences. Hereby, the table forces and torques are already in table coordinates, the forces acquired by the systems (R), (1b) and (2b) must be transformed to table coordinates, and the moments calculated by the known lever.

Finally, Table 3 presents the resulting stiffness matrices for the three variants of the clamping table determined by the three methods calculation, simulation, and experiment. All approaches show realistic results in a similar range. When compared to the experiment, both theoretical approaches lead to higher stiffness values, because not all influences, such as gaps, are modelled.

As main result, the integration of force sensors into the presented rigid framework leads to a stiffness reduction of 45% (experiment). The analytic calculation gives an equal result with 44.9%, and the FE simulation a slightly higher value with 57.2%. Flexure hinges on the other hand, reduce the stiffness by 3.6% (experiment), 2.9 %(calculation) or 8.5 % (simulation), respectively.

Table 3. Comparison of analytical, simulative and experimental determined stiffness matrices $\widehat{K}_T$ in N/µm of the clamping table in the configurations oSoH, wSoH, wSwH

Experiment (Laser)

oSoH:

66	2	3	1	-11	-16
-6	80	38	10	3	1
3	21	202	29	0	-9
2	11	29	12	-1	-2
-13	3	2	-1	14	3
-14	0	-4	-1	1	20

$\xrightarrow{-45{,}0\,\%}$

wSoH:

32	2	0	0	-5	-8
-2	41	20	5	1	0
1	16	112	19	0	-2
1	6	18	7	-1	-1
-6	2	1	0	8	0
-8	-1	-1	0	0	10

$\xrightarrow{-3{,}6\,\%}$

wSwH:

29	3	1	1	-5	-9
-1	40	19	6	1	-1
0	16	102	19	1	-2
1	6	17	7	0	-1
-5	1	1	0	8	0
-6	-1	-1	0	0	9

Calculation (Analytic)

oSoH:

55	0	1	0	-12	-13
0	78	41	12	0	0
1	41	258	48	-1	0
0	12	48	17	0	0
-12	0	-1	0	22	-1
-13	0	0	0	-1	17

$\xrightarrow{-44{,}9\,\%}$

wSoH:

30	0	1	0	-6	-7
0	43	24	7	0	0
1	24	140	26	-1	0
0	7	26	9	0	0
-6	0	-1	0	12	-1
-7	0	0	0	-1	9

$\xrightarrow{-2{,}9\,\%}$

wSwH:

29	0	1	0	-6	-7
0	42	23	7	0	0
1	23	136	25	-1	0
0	7	25	9	0	0
-6	0	-1	0	12	-1
-7	0	0	0	-1	9

Simulation (FEM)

oSoH:

83	1	1	0	-19	-19
1	116	50	16	0	0
1	56	389	71	-1	0
0	18	71	26	0	0
-19	0	-1	0	34	0
-20	0	0	0	1	25

$\xrightarrow{-57{,}2\,\%}$

wSoH:

35	0	1	0	-7	-8
0	49	25	8	0	0
1	28	162	30	-1	0
0	8	30	11	0	0
-7	0	-1	0	14	-1
-8	0	0	0	0	10

$\xrightarrow{-8{,}5\,\%}$

wSwH:

32	0	1	0	-6	-7
0	45	23	7	0	0
1	25	148	27	-1	0
0	8	27	10	0	0
-6	0	-1	0	13	-1
-7	0	0	0	0	10

The FE simulation approach proves itself as time consuming in modelling and simulation as well as expensive with regard to the computational costs. Further, the results are sensitive with respect to details in modelling, parametrisation and meshing. Not all necessary parameters are easy to obtain. Where the longitudinal stiffness of the force sensors can be taken from the datasheet, the lateral stiffness has been acquired from separate experiments. Also, the clamping within the spherical bearings and the screw connections are hard to model sufficiently. With regard to the differences to the experimental results and the good correlation of the simple analytic results, on the other hand, the efforts of FE simulations are not appropriate for the presented application.

4. CONCLUSION

In conclusion, force sensor integration into rigid steel frameworks reduce the stiffness of the framework by 45%, and the insertion of flexure hinges by another approx. 3.6% for the presented setup and application. For the fast evaluation of the compliance of bar frameworks, the classic analytic approach by spring networks is sufficient, whereas FE simulations requests disproportionally higher efforts (minutes compared to weeks), while not leading to better results. The presented experiments show a straightforward approach to

measure spatial compliances of components in an assembled situation by multiple absolute laser interferometers that is also suitable for other applications.

ACKNOWLEDGEMENTS

SYMBOLS AND ABBREVIATIONS

The following symbols and abbreviations are used in this manuscript:

$\{\cdot\}$	Coordinate frame: B: Base, T: Table, H: Up joint, S: Low joint, L: Laser, R: Reflector,
$^{B}(\cdot)_{T}$	Coordinate vector/tensor: top left reference frame, bottom right body frame,
$(\hat{\cdot})$, $(\check{\cdot})$	Estimated values, and measured values,
$(\cdot)^{-T}$	Transposed inverse,
q, x, l	Force sensor coordinates, Cartesian coordinates, and laser coordinates,
f_{q}, f_{x}	Measured forces, and Cartesian forces,
J_{T}, J_{L}	Jacobian of the table framework, and Jacobian of the laser configuration,
$\Delta \underline{x}_{T}$, $^{B}o_{T}$, $^{B}R_{T}$	Pose, position, and orientation of the table platform in the base frame,
K_{q}, K_{x}	Stiffness matrix in sensor coordinates, and in Cartesian coordinates,
N_{q}, N_{x}	Compliance matrix in sensor coordinates, and in Cartesian coordinates,
oSoH	Framework design without sensors and without flexure hinges,
wSoH	Framework design with sensors and without flexure hinges,
wSwH	Framework design with sensors and with flexure hinges.

REFERENCES

[1] FERRARESI C., PASTORELLI S., ZHMUD M.S.N., 1995, *State and Dynamic Behavior of a High Stiffness Stewart Platform-Based Force/Torque Sensor*, Journal of Robotic Systems, 12/12, 883–893.
[2] GAILLET A., REBOULET C., 1983, *An Isostatic Six Component Force and Torque Sensor*, Proceedings of the 13th International Symposium on Industrial Robotics, 102–111.
[3] KERR D., 1989, *Analysis, Properties, and Design of a Stewart-Platform Transducer*, Journal of Mechanisms, Transmissions, and Automation in Design, 111/1, 25–28.
[4] LI F., 1998, *Design and Analysis of a Fingertip Stewart Platform Force/Torque Senso,* PhD Thesis, Simon Fraser University.
[5] NGUYEN C.C., ANTRAZI S., ZHOU Z.-L., 1991, *Analysis and Implementation of a 6 DOF Steward Platform-Based Force Sensor for Passive Compliant Robotic Assembly*, IEEE Proceedings of the SOUTHEASTCON '91, 880–884, DOI: 10.1109/SECON.1991.147886.
[6] SORLI M., PASTORELLI S., 1995, *Six-Axis Reticulated Structure Force/Torque Sensor with Adaptable Performances*, Mechatronics, 5/6, 585–601.
[7] DWARAKANATH T., DASGUPTA B., MRUTHYUNJAYA T., 2001, *Design and Development of a Stewart Platform Based Force–Torque Sensor*, Mechatronics, 11/7, 793–809.

[8]   HUDLEMEYER A.A., NAUGHTON J.W., 2009, *A Hexapod-Based Thrust Balance*, 47th AIAA Aerospace Sciences Meeting Including the New Horizons Forum and Aerospace Exposition, 795.

[9]   KANG C.-G., 2001, *Closed-Form Force Sensing of a 6-Axis Force Transducer Based on the Stewart Platform*, Sensors and Actuators A: Physical, 90/1, 31–37.

[10]   AGHILI F., BUEHLER M., HOLLERBACH, J.M., 2001, *Design of a Hollow Hexaform Torque Sensor for Robot Joints*, I. J. Robotics Res., 20, 967–976.

[11]   DWARAKANATH T., BHUTANI G., 2011, *Beam Type Hexapod Structure Based Six Component Force/Torque Sensor*, Mechatronics, 21/8, 1279–1287, ISSN 0957-4158.

[12]   RÖSKE D., 2002, *Investigation of Different Joint Types for a Multi-Component Calibration Device Based on a Hexapod Structure*, VDI BERICHTE, 1685, 27–36.

[13]   RÖSKE D., 2003, *Metrological Characterization of a Hexapod for a Multi-Component Calibration Device*, XVII IMEKO World Congress (Metrology in the 3rd millennium), 347–351.

[14]   NITSCHE J., BAUMGARTEN S., PETZ M., RÖSKE D., KUMME R., TUTSCH R., 2017, *Measurement Uncertainty Evaluation of a Hexapod-Structured Calibration Device for Multi-Component Force and Moment Sensors*, Metrologia, 54/2, 171.

[15]   RÖSKE D., 2008, *Multi-Component Measurements of the Mechanical Quantities Force and Moment*, Fachorgan für Wirtschaft und Wissenschaft Amts-und Mitteilungsblatt der Physikalisch-Technischen Bundesanstalt Braunschweig und Berlin, 118, 2-3, 56–59.

[16]   DESOGUS S., GERMAK A., MAZZOLENI F., QUAGLIOTTI D., BARBATO G., BARBIERI A., BIGOLIN G., BIN C., 2010, *Developing Multicomponent Force Transducers at INRiM*, IMEKO World Congress, 17–19.

[17]   GENTA G., GERMAK A., BARBAT G., LEVI R., 2016, *Metrological Characterization of an Hexapod-Shaped Multicomponent Force Transducer,* Measurement, 78, 202–206.

[18]   GENTA G., PRATO A., MAZZOLENI F., GERMAK A., GALETTO M., 2018, *Accurate Force And Moment Measurement in Spring Testing Machines by an Integrated Hexapod-Shaped Multicomponent Force Transducer*, Measurement Science and Technology, 29/9, 095902.

[19]   PALUMBO S., GERMAK A., MAZZOLENI F., DESOGUS S., BARBATO G., 2016, *Design and Metrological Evaluation of the New 5 MN Hexapod-Shaped Multicomponent Build-Up System*, Metrologia, 53/3, 956.

[20]   MATICH S., HESSINGER M., KUPNIK M., WERTHSCHÜTZKY R., HATZFELD C., 2017, *Miniaturized Multiaxial Force/Torque Sensor with a Rollable Hexapod Structure*, TM-Technisches Messen, 84, 138–142.

[21]   SEIBOLD U.S. 2013, *An Advanced Force Feedback Tool Design for Minimally Invasive Robotic Surgery*, PhD thesis, Technische Universität München.

[22]   OELHYDRAULIK HAGENBUCH AG, 2017, *Kräfte messen mit Hexamove-Konzept*, Produktprospekt: Hexamove – Bewegung leichtgemacht, 16, 17–17.

[23]   FRIEDRICH C., GROSSMANN K., 2016, *Strukturintegrierte Kraftmessung, Teil 3 - wirkstellenferne Messung*, ZWF, 1–2, 36–40.

[24]   FRIEDRICH C., IHLENFELDT S., 2021, *Model Calibration for a Rigid Hexapod-Based End-Effector with Integrated Force Sensors*, MDPI Sensors, 21/10, 3537, https://doi.org/10.3390/s21103537.

[25]   FRIEDRICH C., KAUSCHINGER B., IHLENFELDT S., 2019, *Spatial Force Measurement Using a Rigid Hexapod-Based End-Effector with Structure-Integrated Force Sensors in a Hexapod Machine Tool*, Measurement, 145C, 350–360.

[26]   FRIEDRICH C., KAUSCHINGER B., IHLENFELDT S., 2020, *Stiffness Evaluation of a Hexapod Machine Tool with Integrated Force Sensors*, Journal of Machine Engineering, 20/1, 58–69.

[27]   FRIEDRICH C., KAUSCHINGER B., IHLENFELDT S., 2016, *Decentralized Structure-Integrated Spatial Force Measurement in Machine Tools*, Mechatronics, 40, 17–27.

[28]   ETALON-AG, 2021, *Absolute Multiline Technology*, https://www.etalonproducts.com/produkte/absolute-multiline-technologie/ (03.11.2021).

[29]   CHEN S.-F. AND KAO I., 2000, *Conservative Congruence Transformation for Joint and Cartesian Stiffness Matrices of Robotic Hands Fingers*, The International Journal of Robotics Research, 19/9, 835–847.

[30]   KREFFT M., 2006, *Aufgabenangepasste Optimierung von Parallelstrukturen für Maschinen in der Produktionstechnik*, PhD thesis, TU Braunschweig.